12

Influence of Fault Strength on Precursory Processes During Laboratory Earthquakes

François. X. Passelègue[1,2], Soumaya Latour[1], Alexandre Schubnel[1], Stefan Nielsen[3], Harsha S. Bhat[4], and Raúl Madariaga[1]

ABSTRACT

Recent seismological observations have highlighted increasing foreshock activity preceding the failure of large earthquakes. Foreshock sequences seem to be the signature of a precursory slip during the nucleation of earthquakes, as observed both prior the Tohoku-Oki Mw 9.0 and the recent Iquique 2014 Mw 8.1 earthquakes. Advances in laboratory experiments allow researchers to reproduce seismic ruptures and to study the earthquake nucleation phase. Here, we track the occurrence of precursory activity prior to stick-slip instabilities in crustal rocks. An exponential acceleration of the precursory slip is systematically observed. This exponential growth implies that (i) the nucleation phase has a characteristic time, (ii) the amount of precursory slip scales with the fracture energy of the fault,and (iii) the moment released seismically by foreshocks also increases exponentially with increasing fault strength. In summary, under upper crustal conditions, the intensity of precursory processes scales with the fracture energy of the largest asperity, which is eventually going to rupture. The larger the fracture energy of the main asperity, the larger the amount of precursory slip and the larger the amount of precursory slip released seismically.

12.1. INTRODUCTION

Recent seismological observations have highlighted increasing foreshock activity preceding the failure of large earthquakes [*Jones and Molnar*, 1976; *Abercrombie and Mori*, 1996; *Bouchon et al.*, 2011; *Kato et al.*, 2012; *Bouchon et al.*, 2013; *Ruiz et al.*, 2014]. Foreshock sequences seem to be the signature of a precursory slip during the nucleation of earthquakes, as observed prior to both the Tohoku-Oki Mw 9.0 [*Kato et al.*, 2012] and the recent Iquique 2014 Mw 8.1 earthquakes [*Ruiz et al.*, 2014; *Kato and Nakagawa*, 2014]. However, foreshocks sequences are not systematic [*Bouchon et al.*, 2013], and the reason why they occur remains poorly understood. Earthquakes are generated because fault strength drops with increasing slip and slip-rate. Using either slip-weakening [*Ida*, 1972; *Campillo and Ionescu*, 1997; *Uenishi and Rice*, 2003] or rate- and state-dependent friction laws [*Dieterich*, 1979; *Ruina*, 1983], theoretical and numerical models show that dynamic rupture is preceded by a nucleation phase during which the rupture grows and accelerates on a localized portion of the fault [*Ida*, 1972; *Campillo and Ionescu*, 1997; *Uenishi and Rice*, 2003; *Dieterich*, 1979; *Ruina*, 1983]. This behavior has already been observed during laboratory experiments under low normal stress conditions [*Ohnaka*, 2003; *Nielsen et al.*, 2010; *McLaskey and Kilgore*, 2013; *Latour et al.*, 2013] and under upper crustal conditions, with the observations of premonitory slip and foreshocks sequence [*Thompson et al.*, 2009; *Goebel et al.*, 2013; *McLaskey and Lockner*, 2014; *Kwiatek et al.*, 2014]. These results suggest that if a similar nucleation stage exists along natural faults, the

[1] *Laboratoire de Géologie, CNRS, École Normale Supérieure, Paris, France*
[2] *University of Manchester, Manchester, UK*
[3] *Durham University, Durham, UK*
[4] *Institut de Physique du Globe de Paris, Paris, France*

Fault Zone Dynamic Processes: Evolution of Fault Properties During Seismic Rupture, Geophysical Monograph 227,
First Edition. Edited by Marion Y. Thomas, Thomas M. Mitchell, and Harsha S. Bhat.

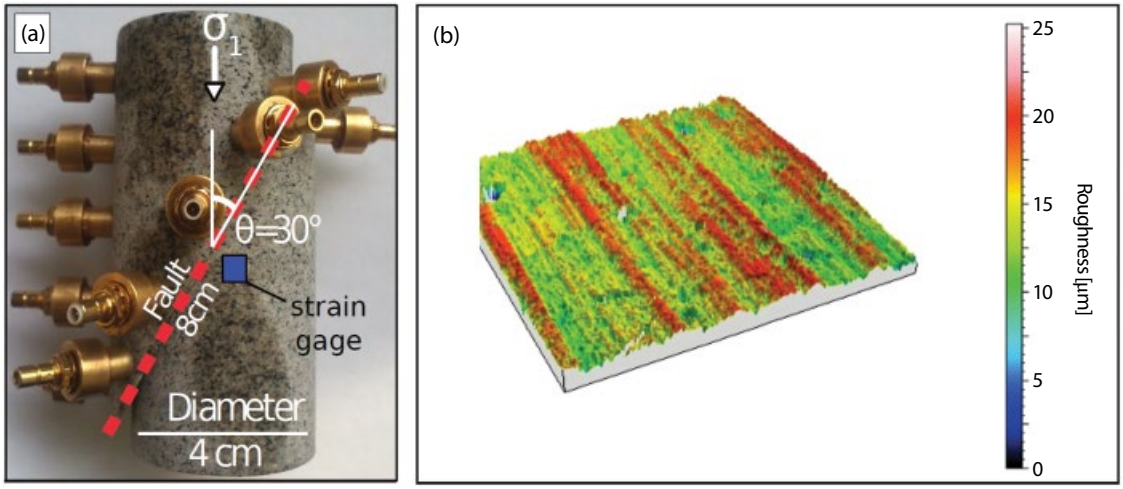

Figure 12.1 Experimental setup. (a) The fault system is simulated using a saw cut Westerly granite sample. The fault is inclined at an angle $\Theta = 30°$ to σ_1. Blue square refers to the location of the strain gauges used to estimate the friction coefficient at the onset of instability and the dynamic stress change. (b) Measurement of the initial roughness of the fault surface. *See electronic version for color representation*.

deformation processes prior the dynamic rupture could be detectable by the records of foreshocks or slow slip events. While it remains difficult to unravel the physical processes using seismological or geodesic observations, laboratory experiments allow the measurement of rupture processes occurring under controlled conditions. Therefore, they can give us good insight into the physical processes leading or not to foreshock activity. Experiments conducted under a broad range of stresses, fault geometries, and rheologies could allow us to understand the physical meaning of these deformation processes observed in nature before earthquakes.

In this chapter, we present results from experiments performed on saw cut Westerly granite samples (Figure 12.1a) submitted to triaxial loading, at conditions representative of the upper crust under various confining pressures (10 to 100 MPa), and covering the range of pressure investigated using biaxial experiments [*Ohnaka*, 2003; *Nielsen et al.*, 2010; *McLaskey and Kilgore*, 2013; *Latour et al.*, 2013] and triaxial experiments [*Thompson et al.*, 2009; *Goebel et al.*, 2013; *McLaskey and Lockner*, 2014; *Kwiatek et al.*, 2014]. The confining pressure is a free parameter in this study, allowing us to understand the influence of the stress acting on the fault and the nucleation processes of laboratory earthquakes.

12.2. EXPERIMENTAL SETUP

12.2.1. The Triaxial Loading Cell

The apparatus used here is a triaxial oil-medium loading cell ($\sigma_1 > \sigma_2 = \sigma_3$) built by Sanchez Technologies. The apparatus can support a confining pressure of 100 MPa and up to 600 MPa in differential stress (for 40 mm sample diameter). The confining pressure ($\sigma_2 = \sigma_3$) and the axial stress (σ_1) are servo-controlled independently. Experiments are conducted by imposing a constant strain rate, ranging from 10^{-5}/s to 10^{-4}/s. Fault displacement was measured externally by capacitive displacement gap sensors.

12.2.2. Sample Preparation

A sample consists in a cylinder of granite presenting a diameter of 40 mm and a length of 88 mm. The basal areas are ground first with a surface grinder to assure maximal perpendicularity to the long axis of the sample. Then the cylinder is cut at an angle of 30 degrees to create a weak fault interface (Figure 12.1a) so that the experimental fault is elliptical, 40 mm in width and 80 mm in length along strike (Figure 12.1a). The fault surface is polished with a surface grinder and then roughened with 240# grit paper to insure constant roughness conditions at the beginning of each experiment. The roughness characterized using laser interferometry is approximately of +/-12.5 μm (Figure 12.1b). Once assembled, the sample is insulated from the confining oil medium by a neoprene jacket 125 mm long and of 50 mm wall thickness. To record acoustic emissions during experiments, the jacket is perforated by 16 holes of 7 mm diameter. The position of each hole is measured accurately to obtain relative sensor locations. Piezoelectric sensors are glued on the rock surface using cyanocrylate adhesive. The sealing between the jacket and the sensors is provided by two layers of flexible and nonbrittle adhesive (Loctite 9455 Hysol). Sixteen P sensors are used in this study (Figure 12.1a).

12.2.2.1. Strain Gauges

In order to remove the deformation of the apparatus (i.e., of the column), external data are compared with the axial deformation measured on the sample using strain gauges. Up to four pairs of strain gauges were used during each experiments. Each pair of strain gauges is composed of two resistances ($\Omega = 120$ ohms) measuring respectively the axial and the radial strain, corresponding to ε_1 and ε_2 in the selected referential. Stresses, axial displacement, and strains are recorded continuously at a sampling rate of 10 to 1000 Hz. The measurement of the dynamic stress-strain change is not possible with these devices since the duration of the rupture propagation is too short (<20 μs) [*Passelègue et al.*, 2013]. However, strain gauge data give us good estimates of the sample elastic constants. During the inelastic parts, they can thus be used as a "low-frequency and near-field" stress gauge, enabling us to infer near-field friction, for instance. Using the axial strain gauge measure, the external measurement of the axial displacement can be corrected for the stiffness of the apparatus using the relation

$$\varepsilon_{ax}^{FS} = \varepsilon_{ax}^{sample} + \frac{\Delta\sigma}{E_{ap}}, \tag{12.1}$$

where ε_{ax}^{FS} is the average axial strain measured on gap sensors, $\varepsilon_{ax}^{sample}$ is the real axial strain of the sample, $\Delta\sigma$ is the differential stress, and E_{ap} is the rigidity of the apparatus. The rigidity of the apparatus is estimated by comparing the axial strain (using strain gauges) during the elastic part of the experiment with the external measurement of the axial displacement using gap sensors. In addition, using linear elastic theory, strain measurements can provide a good estimate of the local static stress changes during experiments. However, as said before, the full capture of the dynamic stress change requires a higher sampling rate.

12.2.3. High-Frequency Stress Measurement

In addition to classical strain gauges, up to four complete Wheatstone bridge strain gauges (referred to as dynamic stress gauge hereafter) were glued directly on the rock sample close to the fault plane (Figure 12.1a, strain gauge). Each dynamic stress gauge is composed of four resistors ($\Omega = 350$ ohms) measuring together the differential strain $\varepsilon_1 - \varepsilon_3$. The signal is relayed to a custom-designed high-frequency amplifier and then recorded, along with the acoustics, on a 16-channel USB oscilloscope at 10 MHz sampling rate. The dynamic stress gauges are calibrated during the elastic loading before each mainshock, assuming a constant Young modulus (64 GPa) of the rock. The amplified (calibrated) signal thus measures at a high sampling rate the dynamic evolution of the differential stress (i.e., $\sigma_1 - \sigma_3$) during dynamic rupture propagation [*Passelègue et al.*, 2016; *Brantut et al.*, 2016]. Measurements of the dynamic stress evolution at high sampling rate have been conducted during experiments WGsc16 and WGsc17 only (Table 12.1).

12.2.3.1. Passive Record of Acoustic Emissions (AEs)

The piezo-ceramic sensors used consist of a PZT crystal (PI ceramic PI255, 5 mm in diameter and 0.5 mm in thickness) encapsulated within a brass casing. All the piezoelectric crystals are polarized in the same way and record preferentially compressional waves. Different ways of recording are used independently or coupled (Figure 12.2). First, the unamplified signal is relayed to

Table 12.1 List of stick-slip experiments presented in this study.

Experiments	P_c (MPa)	Final Axial Shortening (mm)	Peak Shear Stress at First Event (MPa)	Dynamic Strain Gauge	Continuous AE Recording	Number of STE
WGsc3	10	4	8.58	—	—	129
WGsc4	30	2.3	21.5	—	—	42
WGsc5	50	8.4	98.9	—	—	18
WGsc6	50	6.6	82.1	—	—	10
WGsc7	40	5.5	62.1	—	—	4
WGsc9	40	7.3	59.8	—	yes	15
WGsc16a	10	—	12.6	yes	—	3
WGsc16b	30	—	33	yes	—	5
WGsc16c	50	—	47.3	yes	—	13
WGsc16d	100	—	154.5	yes	yes	5
WGsc17a	10	—	8.9	yes	—	1
WGsc17b	20	—	18.6	yes	—	13
WGsc17c	40	—	43.1	yes	—	10
WGsc17d	70	—	72.6	yes	yes	9

Note: AE = acoustic emission; STE = stick-slip events.

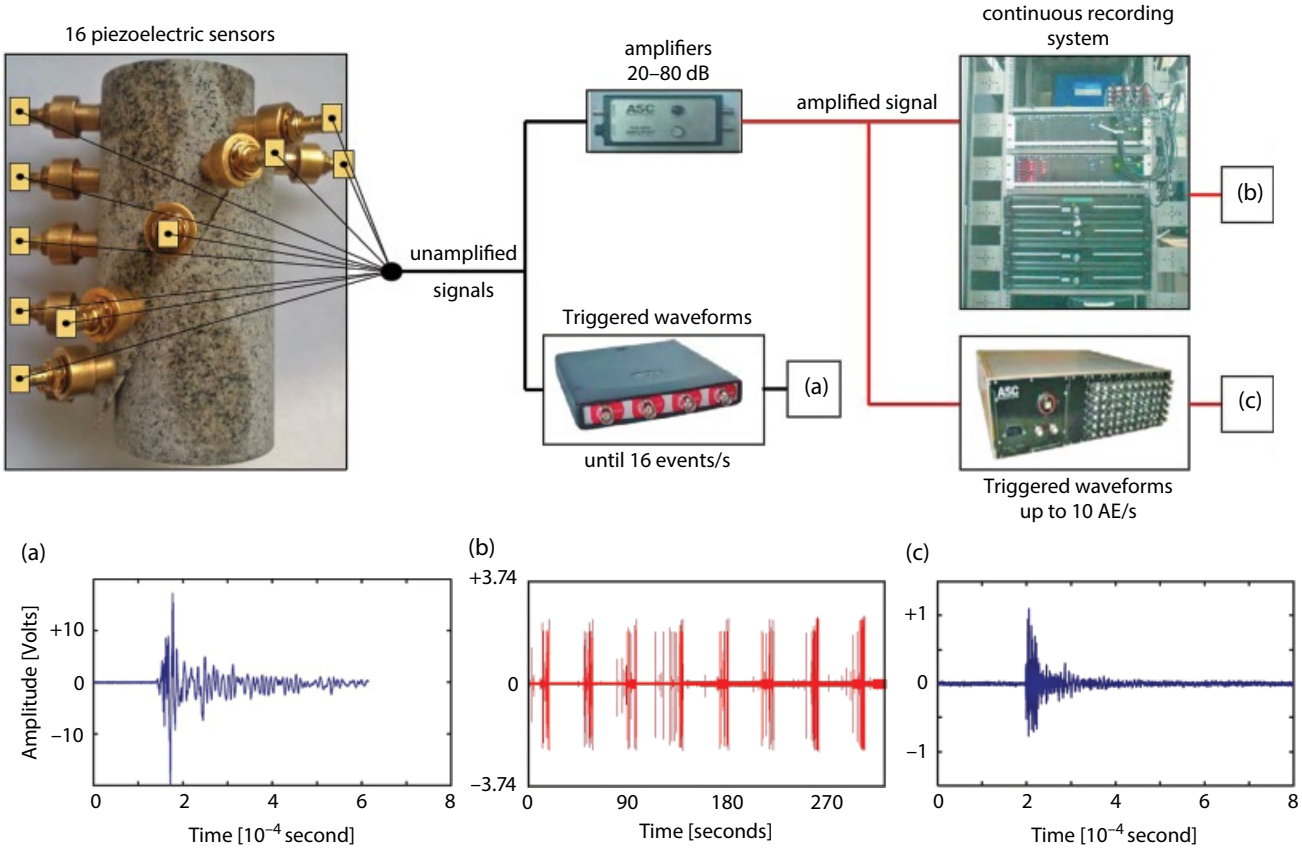

Figure 12.2 Schematic diagram of the AE recording system. Most of the signals are recorded twice, using a digital 16-channel USB oscilloscopes (triggered data) and a 16-channel continuous recorder (continuous data). Foreshock signals are amplified at 45 dB prior to recording, allowing the detection of small events.

a 16-channel digital oscilloscope at a sampling rate of 10 MHz (Figure 12.2a and d). Recording is triggered, on a single arbitrary channel, by the macroscopic dynamic rupture (i.e., rupture of the entire fault) during the experiments [*Schubnel et al.*, 2011; *Passelègue et al.*, 2013].

Using a second system, signals are amplified at 45 dB via 16 preamplifiers. The amplified signals are then relayed to a trigger logic box and, if verifying a given pattern (i.e., a threshold amplitude on a given number of channels in a given time window), are relayed to and recorded by a second 16-channel oscilloscope at 10 MHz sampling rate. In this case, the amplified signals allow the recording of small events before or after the macroscopic events (Figure 12.2b and e). In addition, some stick-slip experiments have been conducted using continuous recording of the acoustic waveforms during the entire experiment at 4 MHz sampling rate (Figure 12.2c and f). The complete waveforms are then analyzed and harvested into single AE again when the signals verify a given pattern. This system is used to record the complete AE waveforms catalogs during experiments while the "triggered data system" (Figure 12.2b and e) is limited to 10 AEs/second. In total, a catalog of more than 200 Stick-slip Events (STE or mainshock) was obtained. Using a continuous AE monitoring, approximately 900 foreshocks were recorded and located for 30 STE or mainshocks, which were preceded by a foreshock sequence. The stress conditions were imposed to mimic those of the upper crust. Normal stress acting on the fault ranged from 15 to 110 MPa. Shear stress and normal stresses on the fault are estimated using the measurements of σ_1 and σ_3, assuming Mohr circle relationships.

12.3. EXPERIMENTAL RESULTS

12.3.1. Mechanical and Acoustic Results

The configuration used in this study is such that when the axial stress is increased, both the normal (σ_n) and the tangential stress (τ) acting on the fault increase. When the state of stress reaches a critical value corresponding to the peak of stress of the fault τ_c, instabilities occur, leading to a macroscopic friction drop (τ/σ_n) (Figure 12.3).

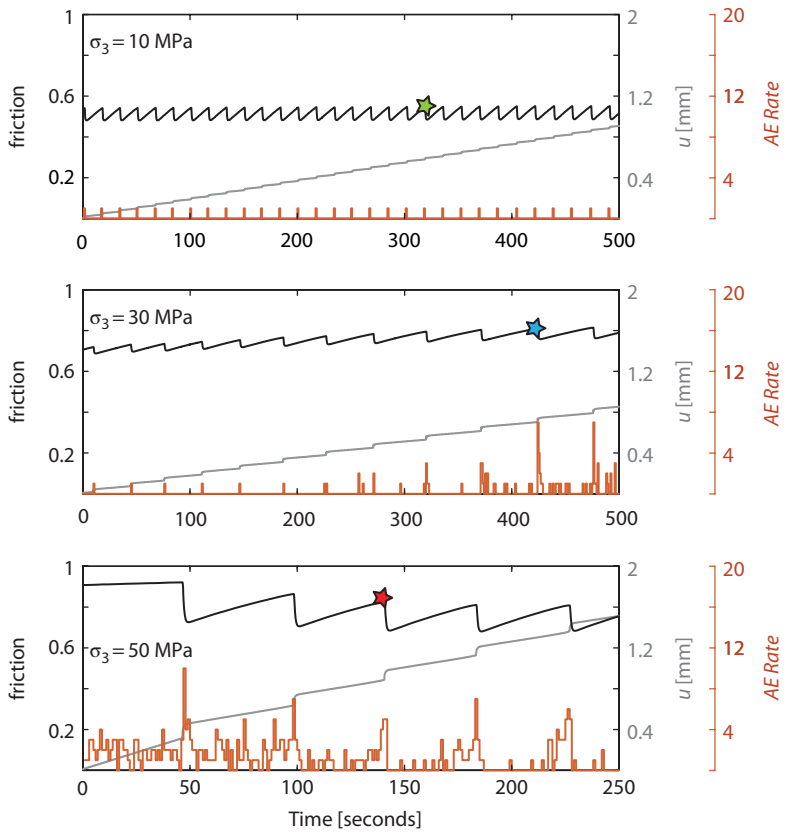

Figure 12.3 Evolution of resolved friction coefficient, displacement, and acoustic emissions rate during stick-slip sequences conducted at 10, 30, and 50 MPa confining pressure. Black, grey, and red solid lines correspond respectively to the friction coefficient, the axial displacement, and the AE-rate (AE/s). Colored stars refer to individual main shocks presented in Figure 12.4. *See electronic version for color representation.*

Three STE sequences at 10, 30, and 50 MPa of confining pressure are displayed in Figures 12.3a, b, and c, respectively. Experimental results highlight that (i) the static friction coefficient, (ii) the stress drop, and consequently, (iii) the moment magnitude (and total seismic slip) and the rupture speed of the mainshock systematically increase with increasing the confining pressure, i.e., the critical shear stress τ_c at the onset of rupture [*Passelègue et al.*, 2013]. Increasing confining pressure also leads to an increase of the acoustic activity. At low confining pressure ($\sigma_3 = 10$ MPa), a single acoustic emission is recorded per stick-slip cycle, and this AE corresponds to the mainshock. However, increasing the confining pressure ($\sigma_3 = 30$ or 50 MPa) leads to an increase of the acoustic activity during stick-slip cycle. The peak of activity is systematically observed in the second preceding the mainshock (Figure 12.3b, c).

The relationship between the frictional behavior of the fault interface and the acoustic activity is presented in Figure 12.4, for three individual events of each STE sequence presented in Figure 12.3. For low values of τ_c (<40 MPa), no foreshocks are recorded, although slip acceleration along the fault is observed (Figure 12.4a). This result suggests that most of the precursory slip is aseismic or that AEs amplitudes are below the threshold of the acoustic monitoring system. In addition, slip strengthening behavior is observed on the fault (i.e, friction increases continuously with fault slip) up to the occurrence of the main shock.

For higher values of τ_c (>40 MPa), we systematically record foreshocks (Figure 12.4b, c). Contrary to the behavior observed for low values of τ_c (<40 MPa), friction measurement (τ_c / σ_n) departs significantly from linearity in the few seconds preceding the mainshock, indicating a local stress release, which coincides both with the occurrence of foreshocks and fault slip acceleration (Figure 12.4b, c). The acceleration in acoustic emission activity corresponds with that of the onset of slip-weakening behavior.

To further investigate the characteristic of foreshock sequences, the acoustic energy released by AEs was estimated similarly to *Zang et al.* [1998] following

$$E_a = \sqrt{\frac{1}{k}\Sigma\left(A_i\right)^2}, \tag{12.2}$$

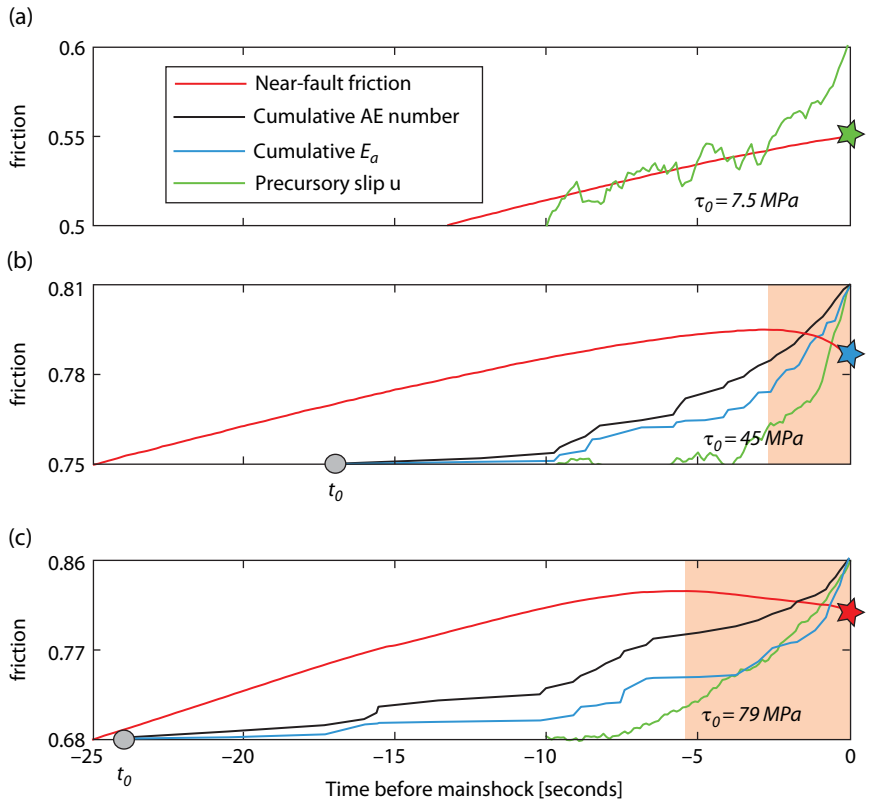

Figure 12.4 Friction and foreshock dynamics at the onset of stick-slip instability. (a, b) Evolution of friction during three isolated stick-slip events under different critical shear stress conditions (colored stars refer to the STE presented in Figure 12.3). The friction is estimated using strain gauges located 3 mm away from the fault plane (Figure 12.1b). The number of AEs, the cumulative acoustic energy (E_a), and the precursory slip are normalized by their final values and vary from 0 to 1. The signal-to-noise ratio increases with increasing final values of precursory slip (as the critical shear stress increases). Final values of precursory slip are respectively 1.3, 3.2, and 9.5 μm for a, b, and c. Background orange area presents the fraction of time under slip weakening regime. Note that this fraction of time increases with τ_c. *See electronic version for color representation*.

where A_i is the maximum amplitude of the AE "i" and k is the number of sensors used for the amplitude calculation. An abrupt acceleration in the cumulative acoustic energy occurs in the few seconds preceding the mainshock. Since the cumulative acoustic energy increases faster than the cumulative AE number, this indicates that the average moment of AEs is getting larger, or in other terms, that the b-value of the Gutenberg-Richter law is decreasing prior to failure, as already observed by several experimental studies [*Sammonds et al.*, 1992; *Goebel et al.*, 2012, 2013; *Kwiatek et al.*, 2014]. In summary, increasing the critical shear stress τ_c in our experiments leads to an increase of (i) the number of foreshocks, (ii) the amount of precursory slip, and (iii) the precursory cumulative acoustic energy release (Figure 12.4). These observations suggest that τ_c controls the intensity of the precursory activity.

12.3.2. Location of Acoustic Emissions

P-wave arrival recorded on each sensor was automatically picked using a simple RMS function (the accuracy of autopicking is on the order of 0.1 μs). Next, to locate AEs, we calculate the theoretical travel times between a possible nucleation point (X,Y,Z) next to the fault plane and each piezoelectric sensor location in the array. We assume a 3D geometry, with a fault thickness of 1 cm, which corresponds to the size of the largest crack observed on the postmortem samples. At a given station k, theoretical P-wave travel times from nucleation point (X,Y,Z) can be calculated following

$$t = \frac{\sqrt{\left(X - X_k\right)^2 + \left(Y - Y_k\right)^2 + \left(Z - Z_k\right)^2}}{C_P}, \qquad (12.3)$$

where C_P is the compressional wave velocity. For each AE event, time residuals Δt, between observed arrival times t^{exp} and theoretical ones t_k, are calculated for different possible initiation times (t_0) following

$$\Delta t = \sqrt{\frac{\sum_{0}^{k} \left| t_k^{exp} - t_k - t_0 \right|}{n}}, \qquad (12.4)$$

where n is the number of experimental arrival times used.

The sum of the residual time is then minimized using a least-square function. The minimization outputs the nucleation point of the event and its time of initiation. The average value of the residual time for all AEs located is about 0.1 µs, corresponding to a location accuracy of 0.5 mm assuming $C_P = 5800$ m / s. This method allows us to remove AEs nucleating far away from the fault. Note, however, that more than 95% of the foreshocks are located within the considered fault thickness.

The distribution of foreshock hypocenters and magnitudes as a function of time along the fault for representative foreshock sequences is presented in Figure 12.5. Initially, most of the foreshocks have low magnitudes and are located at the periphery of the fault surface (Figure 12.5a–c). The average magnitude of foreshocks gradually increases with time, while the hypocenters migrate toward the inner section of the fault plane (Figure 12.5). The strongest foreshock generally occurs just prior to the mainshock (Figure 12.5). In Figure 12.5a, we can also note the presence of clusters, and in particular, the fact that the same foreshock source (or asperity) may be able to break twice within a small time window, sometimes with over one order magnitude difference in moment release.

12.3.3. Dynamic Stress Drop During Mainshocks

The raw data representing the differential stress evolution during a mainshock observed at 50 MPa confining pressure (middle range of pressure explored in this study) is displayed in Figure 12.6a. The stress is stable until the passage of the rupture front. Then, a strong and abrupt decrease of the stress is observed down to a minimum value. The difference between the peak stress and the minimal value corresponds to the dynamic stress change and can be used to estimate the dynamic shear stress drop by considering a 2D geometry. After the drop, frame oscillations are observed

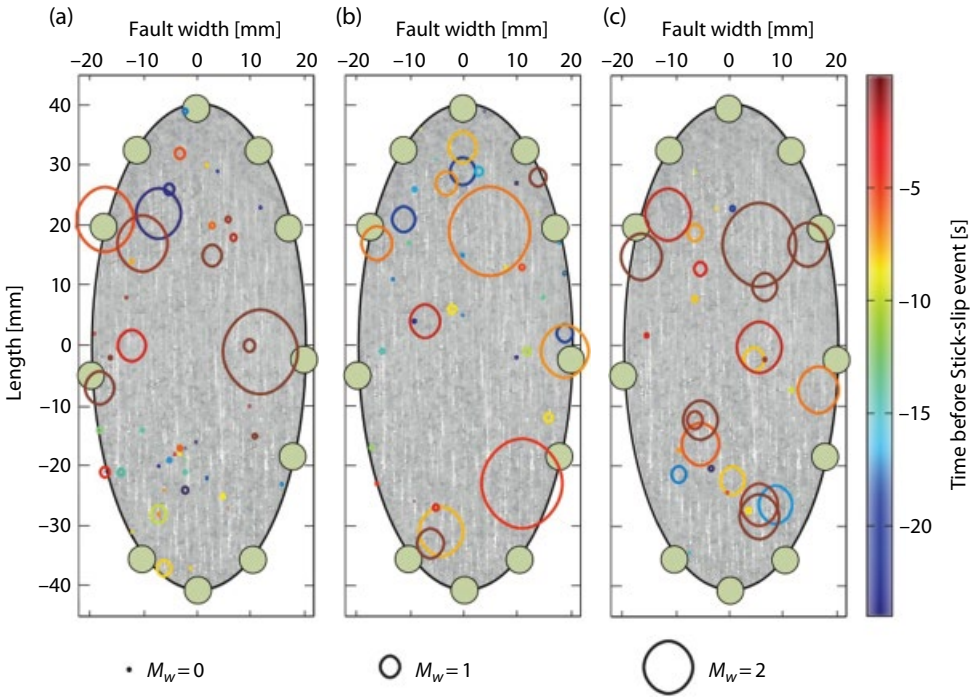

Figure 12.5 Location of foreshock epicenters prior to main shocks. (a–c) Results of the location of foreshocks along the fault plane prior to three main shocks induced at 50 MPa confining pressure. The colored bar corresponds to the initiation time of each foreshock relative to the main shock. Note that one part of the fault (central part) remains devoid of acoustic activity. The background image presents the fault surface striation after the experiment. The marker size corresponds to the relative magnitude of each foreshock. Gray circles around the fault correspond to sensor locations. *See electronic version for color representation*.

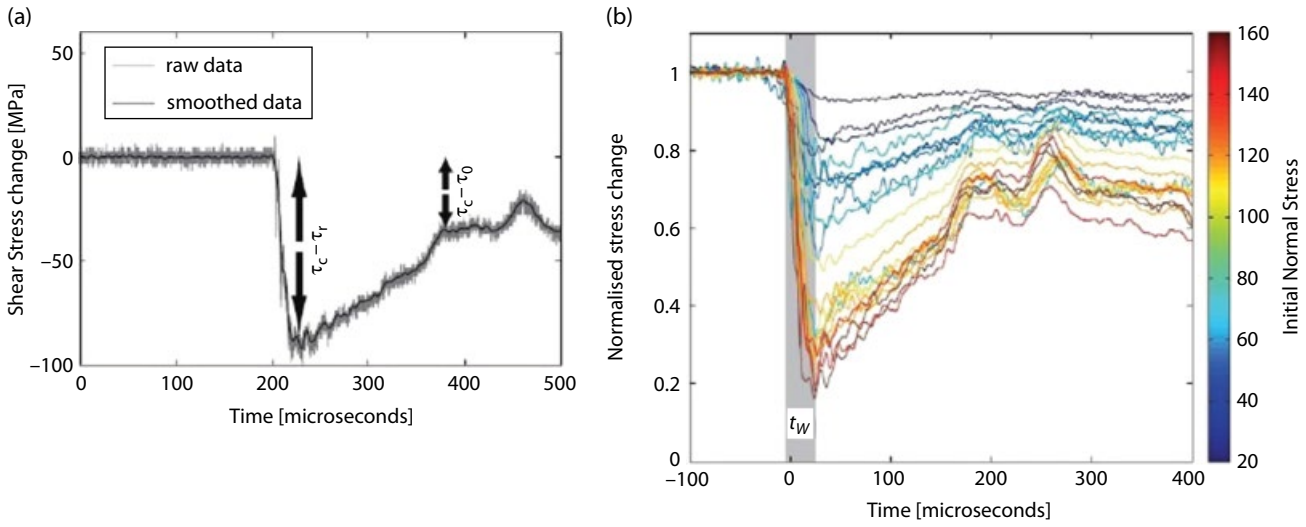

Figure 12.6 High-frequency stress measurements. (a) Evolution of the stress during stick-slip instability at 130 MPa in normal stress. Grey solid line corresponds to raw data. The data have been smoothed using low-pass filter at 200 KHz in order to remove noise (black solid line). A strong dynamic stress drop is first observed. The final stress difference corresponds to the static stress drop. (b) Relative dynamic stress change curves recorded for 20 main shocks. All curves are normalized by the critical shear stress (τ_c) measured at the onset of rupture. Both dynamic and static stress drops increase with the initial state of stress. The weakening time t_w tends to decrease with stress. Stress oscillations after the dynamic stress drop are probably due to resonances of the apparatus frame. *See electronic version for color representation*.

due to the rapid release of stress, which generally occurs in a few microseconds (i.e., the weakening time $t_w \approx 20\mu$ s). The amplitude of the oscillations decreases with time until the stress reaches a stable value (Figure 12.6a), which corresponds to the final stress after instability [*Beeler et al.*, 2012]. The difference between the initial shear stress and the final stress value is consistent with the static stress drop recorded using low sampling rate measurements. All the data presented below have been smoothed using a low-pass filter at 200 KHz in order to remove the high-frequency content related to electrical noise and wave propagation. The influence of the stress acting on the fault on the dynamic strength drop is presented in Figure 12.6b. For low values of critical shear stress ($\tau_c < 20$ MPa), only a fraction of the stress (0.1 τ_c), i.e., of the elastic strain, is released during macroscopic rupture. However, increasing the normal stress acting on the fault leads to an increase of the fraction of the shear stress released during the macroscopic rupture, which can go up to 0.8 τ_c.

12.4. EXPONENTIAL INCREASE OF THE PRECURSORY ACTIVITY

Precursory slip was systematically observed even at low shear stress (Figure 12.7a). The evolution of the precursory slip evolves exponentially with time following

$$u(t) = e^{\frac{t}{t_c}}, \tag{12.5}$$

where t_c is a characteristic time for the nucleation phase, previously defined during laboratory experiments [*Latour et al.*, 2013]. Note that t_c differs from the time to failure. It corresponds to the characteristic time of the exponential, i.e., the tangent at $t = 0$. The time to failure corresponds to the time for the exponential slip to grow up to a critical value after which dramatic slip weakening occurs and the rupture becomes dynamic. In these new experiments, this parameter is between 2 and 4 seconds and is independent of τ_c (Figure 12.7b). These values of t_c were determined from the maximum slip rate measured just prior to main shocks following $\dot{u} = u_c / t_c$. Both values of u_c and $\dot{u}$ increase, with τ_c leading to a same order of magnitude of t_c. This parameter was also found to be independent of the stress in a previous experimental study [*Latour et al.*, 2013]. Predicted by several theoretical and experimental studies [*Ohnaka*, 2003; *Ida*, 1972; *Campillo and Ionescu*, 1997; *Uenishi and Rice*, 2003], this is clear experimental evidence of systematic exponential precursory slip growth, independent of the state of stress and of the friction of the fault interface (here, $0.4 < f < 0.9$). However, the inferred value of t_c is three orders of magnitude larger in this study than in the study of *Latour et al.* [2013], which suggests that this parameter might be a function of the fault geometry and the frictional properties of the fault interface.

The characteristic time t_c of nucleation can be approximated by *Latour et al.* [2013],

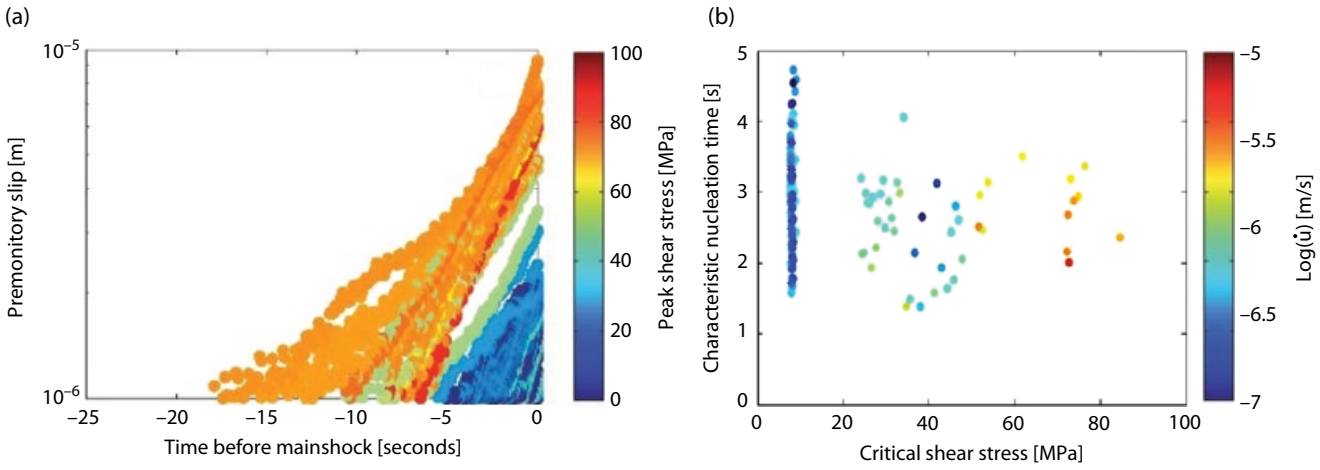

Figure 12.7 Characteristic of the precursory slip. (a) Precursory slip evolution curves of all main shocks. The slip is corrected from elastic effects. The colored bar represents the critical shear stress at the onset of each main shock. Displacement is plotted in logarithmic scale, demonstrating an exponential acceleration of slip prior to the dynamic slip instability. The final value u_c of precursory slip increases with τ_c. (b) Characteristic nucleation time of each main shock as a function of the critical initial shear stress. The colored bar presents the maximal sliding velocity reached during the nucleation. While the characteristic time is independent of stress ($t_c \approx 3$), the peak sliding velocity increases with stress. *See electronic version for color representation*.

$$t_c = \frac{k\mu}{p_0}\frac{D_c}{f_s - f_d}, \tag{12.6}$$

where k is the ratio between the sliding velocity and the rupture velocity, p_0 is a characteristic power density leading to the weakening of the fault surface [*Di Toro et al.*, 2011], D_c is the critical weakening distance, μ is the shear modulus of the granite, and $(f_s - f_d)$ is the friction drop. Using the average values measured directly here for one of the events with the longest foreshock sequence ($(f_s - f_d) \approx 0.02$ during the nucleation phase, Figure 12.4; $D_c \approx u_c \approx 10\ \mu m$, Figure 12.6a; $t_c \approx 3$ s, Figure 12.6b), a typical ratio of sliding velocity versus rupture velocity of 3.10^{-4} [*Latour et al.*, 2013] and of the shear modulus of Westerly granite (34GPa) yields a critical power density p_0 value of $\approx 1700 \pm 150$ W/m^2, which is compatible with a recent experimental compilation of critical power densities [*Di Toro et al.*, 2011]. However, there does not seem to be a systematic relationship between t_c and τ_c (Figure 12.7b). This equation can be written (with $D_c \approx u_c$) as $f_s - f_d = \frac{k\mu u_c}{p_0 t_c}$, assuming further that k and p_0 are independent on τ_c [*Latour et al.*, 2013; *Di Toro et al.*, 2011]. Given that t_c presents same order of magnitude values, the friction drop $(fs - fd)$ increases with τ_c in the same way as u_c.

In addition, normalizing the cumulative acoustic energy $E(t)$ with the final cumulative acoustic energy E_a and time with the duration t_0 of each foreshock sequences, we can show that, when foreshocks are recorded, the precursory acoustic energy also increases exponentially (Figure 12.8):

$$\frac{E(t)}{E_1} = e^{\alpha\frac{(t-t_0)}{t_0}}, \tag{12.7}$$

where α is a scaling constant (the best fit has been determined using $\alpha = 3.47$). This observation demonstrates that the rupture of initially small asperities are followed by the rupture of larger and larger ones, and so on up to the rupture of the main asperity (Figures 12.5c and 12.8).

12.5. INFLUENCE OF STRESS ON THE PRECURSORY ACTIVITY

The critical slip u_c required to trigger the mainshock increases with critical shear stress (Figure 12.7a), which suggests that, for the main asperity, D_c increases with τ_c. To further investigate the influence of τ_c on the fault mechanical properties, we now estimate the effective fracture energy $G = D_c\sigma_n\frac{f_s - f_d}{2}$ of main shocks using the dynamic stress drop records (Figure 12.6). The effective fracture energy (J/m^2) is a known proxy for the strength of the fault [*Wong*, 1982, 1986; *Ohnaka*, 2003]. Assuming a constant rupture velocity (i.e., a constant sliding velocity) and a purely slip weakening behavior, the critical slip distance D_c can be estimated using the equation [*Ida*, 1972; *Palmer and Rice*, 1973; *Rice*, 1979]

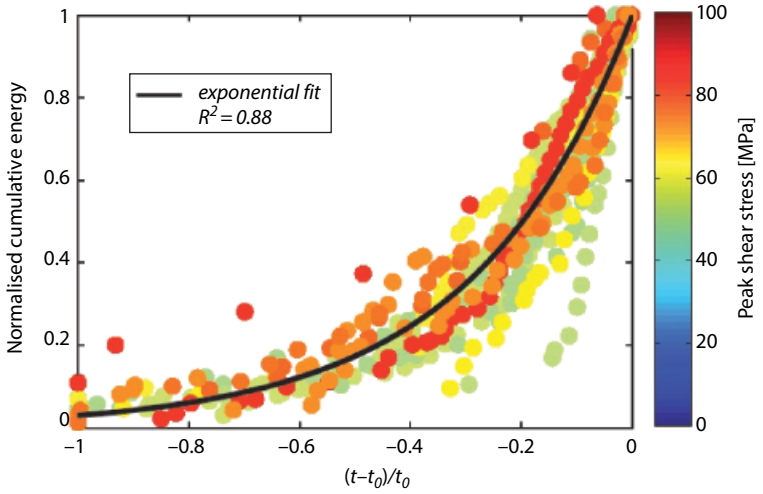

Figure 12.8 Normalized cumulative acoustic energy released as a function of normalized time for 20 stick-slip cycles. Foreshock sequences collapse to an exponential law (black solid line) with $\alpha \approx 3.5$. *See electronic version for color representation.*

$$D_c = \frac{16(1-\nu)}{9\pi}\frac{V_r t_w \sigma_n (f_s - f_d)}{\mu}, \tag{12.8}$$

where μ is the shear modulus of the granite estimated using strain measurements ($\mu = 34\ GPa$).

The value of the rupture velocity V_r at a given point of the fault can be estimated during main shock using the dominant arrival recorded on the near-field sensor records as shown in *Schubnel et al.* [2011] and *Passelègue et al.* [2013]. For simplicity, we approximate the shape of the rupture front by a circular shape at sub-Rayleigh velocity and by an elliptical shape at supershear velocity, where the ratio of the two axes corresponds to the ratio of the velocities in the in-plane direction. Thereafter, the value of the rupture velocity at a given point of the fault can be estimated during the event using

$$V_{r(X,Y)} = \frac{1}{\sqrt{\frac{cos^2\alpha}{C_s^2} + \frac{sin^2\alpha}{V_{II}^2}}}, \tag{12.9}$$

where V_{II} is the rupture velocity along strike and α is the angle between the coordinates of the given point (X, Y) and the mode-III direction (Figure 12.6a). Both sub-Rayleigh and supershear ruptures are observed during experiments [*Schubnel et al.*, 2011; *Passelègue et al.*, 2013].

Using this estimation of the rupture velocity, the values of the dynamic stress drop, and the values of the weakening time t_w (Figure 12.6), the values of D_c and G were estimated for each mainshock. The values of D_c obtained using equation (12.8) can be considered overestimates because our measurements of the stress change are not performed directly on the fault plane [*Svetlizky and Fineberg*, 2014]. However, using this simple relation, D_c remains always smaller than the final displacement, suggesting that this calculation provides good estimates. Both D_c and G increase with τ_c. This result agrees with previous experimental studies [*Wong*, 1986; *Kato et al.*, 2003].

A strong correlation between G and the intensity of the precursory activity is observed. At low critical shear stress ($\tau_c < 20$ MPa), where no foreshocks are observed, G falls between 1 and 10 J/m^2, i.e., close to values for the rupture of single minerals [*Fredrich and Wong*, 1986]. However, a power four dependence of G with critical shear stress is observed, and G reaches values close to 10^4 J/m^2 for the highest value of stress attained during macroscopic rupture (Figure 12.9). In agreement with previous experimental studies [*Wong*, 1982, 1986; *Ohnaka*, 2003], this demonstrates that the strength of the fault increases with the stress acting on the fault plane. This is expected from nucleation length theory [*Ida*, 1972; *Campillo and Ionescu*, 1997; *Uenishi and Rice*, 2003] (Figure 12.9), because the transition between stable slip and dynamic rupture theoretically depends on both normal stress and the fracture energy. Indeed, for a linear slip weakening friction law [*Ida*, 1972; *Campillo and Ionescu*, 1997; *Uenishi and Rice*, 2003], the critical nucleation length can be defined as

$$L_c = 2\beta\frac{\mu G}{\left(\tau_c\left(1-\frac{f_d}{f_s}\right)\right)^2}, \tag{12.10}$$

where β is a nondimensional shape factor coefficient (≈ 1.158) [*Campillo and Ionescu*, 1997]. Asperities of size

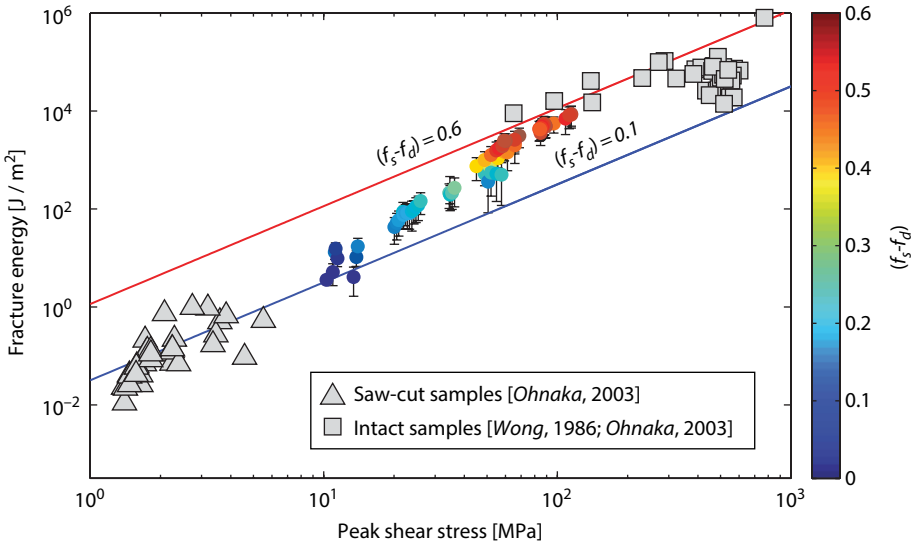

Figure 12.9 Influence of the state of stress on fault strength. Comparison of peak shear stress dependence of fracture energy (G) computed for our experiments with previous experimental results on saw-cut samples [*Ohnaka*, 2003a] and on intact rocks [*Wong*, 1982; *Ohnaka*, 2003a]. The fracture energy is calculated using dynamic stress drop measurements. The colored bar corresponds to the value of the dynamic friction drop. In the background, fracture energy G (solid lines) as a function of critical shear stress τ_c at the transition from stable to dynamic rupture for two values of friction drop (0.6 and 0.1 for red and blue solid lines, respectively). G is calculated following equation (12.4), assuming that $\tau_p = \tau_c$ and considering L equal to the fault length ($L_f = 0.08$m). *See electronic version for color representation*.

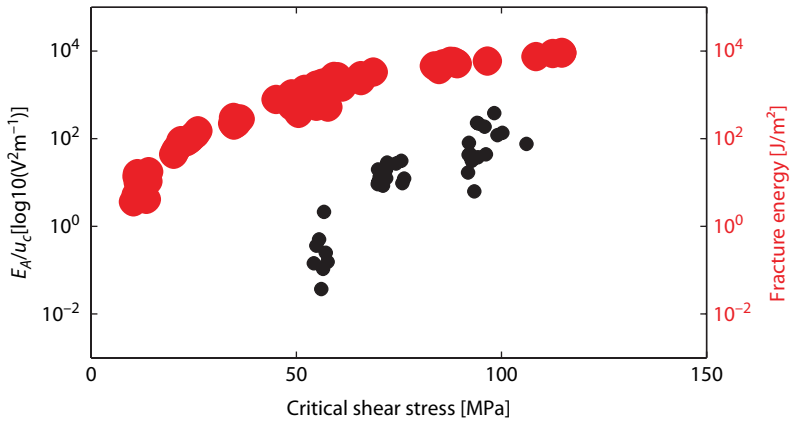

Figure 12.10 Ratio between the acoustic energy and the total precursory moment release measured on the fault ($M_p = \hat{A}\mu u_c S$) as a function of critical shear stress (black circles). In the background, large red circles present values of fracture energy G of main shocks as a function of τ_c (Figure 12.9). Foreshocks are observed when the fracture energy of the main shocks becomes large behind the fracture energy for small minerals. The larger the fracture energy of the main shock, the larger the intensity of the foreshock sequence.

L can slip seismically only if $L > L_c(\tau_c, G)$, otherwise, the slip remains aseismic. Assuming $L_c = L_f$, a power exponent 2 is expected from equation (12.4). In our experiments, a power four dependence of G with respect to τ_c is observed because the friction drop also increases linearly with τ_c [*Passelègue*, 2014; *Passelègue et al.*, 2016].

The precursory acoustic energy release rate κ (V²/m), i.e., the amount of acoustic energy released by foreshocks (E_a, V²) per amount of precursory slip u_c (m), increases with τ_c (Figure 12.10). At low stress, the lack of foreshocks may be due to a technical limit (AE threshold sensibility). However, at higher stresses, the precursory acoustic energy release rate κ increases with increasing critical shear stress, i.e., with increasing fault strength. In other words, the ratio between seismic and aseismic premonitory slip increases with τ_c and G.

12.6. CONCLUSIONS AND IMPLICATIONS FOR NATURAL EARTHQUAKES

Our experimental results demonstrate that premonitory slip is systematically observed during the nucleation stage of mainshocks. This result agrees with previous experimental studies conducted at low stress conditions [*Ohnaka*, 2003; *McLaskey and Kilgore*, 2013; *Latour et al.*, 2013] and under upper crustal stress conditions [*McLaskey and Lockner*, 2014]. We demonstrate that this premonitory slip evolves exponentially up to the dynamic rupture of the entire experimental fault. In addition, this premonitory slip can be (i) mostly aseismic at low stress conditions or (ii) signaled by a sequence of foreshocks, which also evolves exponentially, at higher stress conditions. This observation can be explained by the coupling of two phenomena: (1) at low stress conditions, the fracture energy of the entire fault is comparable to the fracture energy of minerals. In these conditions, the rupture of small asperities could release enough energy to propagate the rupture through the entire fault. On the contrary, under high stress conditions, small asperities can fail seismically without rupturing the entire fault because of the large fracture energy required to propagate the rupture of the entire fault; (2) As expected by equation (12.10), the increase of stress acting along the fault decreases the nucleation length. For small asperities, assuming that the fracture energy scales with the size of the rupture [*Abercrombie and Rice*, 2005], increasing the stress acting on the fault could promote the dynamic failure of small asperities, which would slip aseismically at low stress conditions.

As observed in nature [*Kato et al.*, 2012; *Bouchon et al.*, 2013; *Ruiz et al.*, 2014], foreshock sequences are the signature of a precursory slip during the nucleation of laboratory earthquakes. While no foreshocks are detected at low stress conditions ($\tau_c < 20$ MPa), the trigger of the premonitory slip triggers a foreshock sequence at larger stress conditions. In these conditions, the foreshock activity also evolves exponentially up to the rupture of the mainshock. These experimental results are in agreement with natural observations along the interplate interface [*Bouchon et al.*, 2013] and with the cascade model proposed by *Ellsworth et al*. [2004] and *Beroza and Ellsworth* [1996].

As stated previously, the occurence of foreshock sequences is related to high stress conditions in the laboratory and to the increase of the fracture energy of the experimental fault. Along natural faults, an accurate estimate of the absolute stress is difficult. However, it has been noted that the foreshock activity that preceded the 2011 Tohoku Mw 9.0 earthquake was confined under a certain depth [*Ide and Aochi*, 2013]. The same observation has been reported during the Iquique earthquake [*Ruiz et al.*, 2014]. This might be explained by the fact that at shallow depth the relatively small asperities that may cause foreshocks will not fail dynamically [*Ide and Aochi*, 2013; *Noda and Lapusta*, 2013], because the critical nucleation length L_c is larger than small size asperity.

Of course, many other parameters could play a important role in the premonitory phase of crustal earthquakes. For example, high pore fluid pressures may reduce fault strength, increase the nucleation size, and prevent the occurrence of foreshocks. In addition, at the bottom of the seismogenic layer, intracrystalline plasticity and ductile deformation processes are active [*Brace and Kohlstedt*, 1980] so that again, the nucleation size could be large enough to prevent small asperities from being seismic. Fault geometry will also have a strong influence on the occurrence of foreshocks. Indeed, both the distribution of the sizes of asperities and the way that their effective frictional properties scale up plays an important role in the occurrence of foreshocks. Finally, premonitory slip or stable slip seems to be the necessary condition to observe foreshock sequence. Fault complexity decreases with cumulative slip and fault maturity [*Stirling et al.*, 1996]. Plate boundary faults should be less segmented than intraplate ones and thus promote the occurrence of foreshock sequence induced by stable slip around seismic asperities [*Bouchon et al.*, 2013; *Kato et al.*, 2012; *Ruiz et al.*, 2014].

ACKNOWLEDGMENTS

We acknowledge the technical help of Yves Pinquier (ENS) during the course of the experiments. Mai-Linh Doan (UJF) and Gérard Gary (Ecole Polytechnique) provided the technical drawings for the high-frequency strain gauge amplifier. We thank A. Niemeijer and an anonymous reviewer who helped enhance the quality of the paper, and also three anonymous reviewers who revised an earlier version of the work. This work was partially supported via the ANR program ANR-12-JS06-0003 DELF.

REFERENCES

Abercrombie, R. E., and J. Mori (1996), Occurrence patterns of foreshocks to large earthquakes in the western United States, *Nature*, *381*(6580), 303–307.

Abercrombie, R. E., and J. R. Rice (2005), Can observations of earthquake scaling constrain slip weakening? *Geophysical Journal International*, *162*(2), 406–424.

Beeler, N., B. Kilgore, A. McGarr, J. Fletcher, J. Evans, and S. R. Baker (2012), Observed source parameters for dynamic rupture with non-uniform initial stress and relatively high fracture energy, *Journal of Structural Geology*, *38*(0), 77–89, doi:https://doi.org/10.1016/j.jsg.2011.11.013.

Beroza, G. C., and W. L. Ellsworth (1996), Properties of the seismic nucleation phase, *Tectonophysics*, *261*(1), 209–227.

Bouchon, M., V. Durand, D. Marsan, H. Karabulut, and J. Schmittbuhl (2013), The long precursory phase of most large interplate earthquakes, *Nature Geoscience*, *6*(4), 299–302.

Bouchon, M., H. Karabulut, M. Aktar, S. Özalaybey, J. Schmittbuhl, and M.-P. Bouin (2011), Extended nucleation of the 1999 Mw 7.6 Izmit earthquake, *Science*, *331*(6019), 877–880.

Brace, W., and D. Kohlstedt (1980), Limits on lithospheric stress imposed by laboratory experiments, *Journal of Geophysical Research: Solid Earth (1978–2012)*, *85*(B11), 6248–6252.

Brantut, N., F. X. Passelègue, D. Deldicque, J.-N. Rouzaud, and A. Schubnel (2016), Dynamic weakening and amorphization in serpentinite during laboratory earthquakes, *Geology*, *44*(8), 607–610.

Campillo, M., and I. R. Ionescu (1997), Initiation of antiplane shear instability under slip dependent friction, *Journal of Geophysical Research: Solid Earth (1978–2012)*, *102*(B9), 20,363–20,371.

Di Toro, G., R. Han, T. Hirose, N. De Paola, S. Nielsen, K. Mizoguchi, F. Ferri, M. Cocco, and T. Shimamoto (2011), Fault lubrication during earthquakes, *Nature*, *471*(7339), 494–498.

Dieterich, J. H. (1979), Modeling of rock friction: 1. Experimental results and constitutive equations, *Journal of Geophysical Research: Solid Earth (1978–2012)*, *84*(B5), 2161–2168.

Ellsworth, W. L., M. Celebi, J. R. Evans, E. G. Jensen, R. Kayen, M. C. Metz, D. J. Nyman, J. W. Roddick, P. Spudich, and C. D. Stephens (2004), Near-field ground motion of the 2002 Denali fault, Alaska, earthquake recorded at pump station 10, *Earthquake Spectra*, *20*(3), 597–615, doi:10.1193/1.1778172 .

Fredrich, J. T., and T.-F. Wong (1986), Micromechanics of thermally induced cracking in three crustal rocks, *Journal of Geophysical Research: Solid Earth (1978–2012)*, *91*(B12), 12,743–12,764.

Goebel, T., T. Becker, D. Schorlemmer, S. Stanchits, C. Sammis, E. Rybacki, and G. Dresen (2012), Identifying fault heterogeneity through mapping spatial anomalies in acoustic emission statistics, *Journal of Geophysical Research: Solid Earth (1978–2012)*, *117*(B3).

Goebel, T., D. Schorlemmer, T. Becker, G. Dresen, and C. Sammis (2013), Acoustic emissions document stress changes over many seismic cycles in stick-slip experiments, *Geophysical Research Letters*, *40*(10), 2049–2054.

Ida, Y. (1972), Cohesive force across the tip of a longitudinal-shear crack and griffith's specific surface energy, *Journal of Geophysical Research*, *77*(20), 3796–3805.

Ide, S., and H. Aochi (2013), Historical seismicity and dynamic rupture process of the 2011 Tohoku-Oki earthquake, *Tectonophysics*, *600*, 1–13.

Jones, L., and P. Molnar (1976), Frequency of foreshocks, *Nature*, *262*(5570).

Kato, A., and S. Nakagawa (2014), Multiple slow-slip events during a foreshock sequence of the 2014 Iquique, Chile Mw 8.1 earthquake, *Geophysical Research Letters*, *41*(15), doi:10.1002/2014GL061138.

Kato, A., K. Obara, T. Igarashi, H. Tsuruoka, S. Nakagawa, and N. Hirata (2012), Propagation of slow slip leading up to the 2011 Mw 9.0 *Tohoku-Oki earthquake, Science*, *335*(6069), 705–708.

Kato, A., M. Ohnaka, and H. Mochizuki (2003), Constitutive properties for the shear failure of intact granite in seismogenic environments, *J. Geophys. Res.*, *108*(B1).

Kwiatek, G., T. H. W. Goebel, and G. Dresen (2014), Seismic moment tensor and b value variations over successive seismic cycles in laboratory stick-slip experiments, *Geophys. Res. Lett.*, *41*(16), 5838–5846.

Latour, S., A. Schubnel, S. Nielsen, R. Madariaga, and S. Vinciguerra (2013), Characterization of nucleation during laboratory earthquakes, *Geophysical Research Letters*, *40*(19), 5064–5069.

McLaskey, G. C., and B. D. Kilgore (2013), Foreshocks during the nucleation of stick-slip instability, *Journal of Geophysical Research: Solid Earth*, *118*(6), 2982–2997.

McLaskey, G. C., and D. A. Lockner (2014), Preslip and cascade processes initiate laboratory stick-slip, *Journal of Geophysical Research: Solid Earth*.

Nielsen, S., J. Taddeucci, and S. Vinciguerra (2010), Experimental observation of stick-slip instability fronts, *Geophysical Journal International*, *180*(2), 697–702, doi:10.1111/j.1365-246X.2009.04444.x.

Noda, H., and N. Lapusta (2013), Stable creeping fault segments can become destructive as a result of dynamic weakening, *Nature*, *493*(7433), 518–521.

Ohnaka, M. (2003), A constitutive scaling law and a unified comprehension for frictional slip failure, shear fracture of intact rock, and earthquake rupture, *J. Geophys. Res.*, *108*(B2), 2080.

Palmer, A. C., and J. R. Rice (1973), The growth of slip surfaces in the progressive failure of over-consolidated clay, *Proceedings of the Royal Society of London. A. Mathematical and Physical Sciences*, *332*(1591), 527–548, doi:10.1098/rspa.1973.0040 .

Passelègue, F. X. (2014), Experimental study of the seismic rupture, Ph.D. thesis, École Normale Supérieure de Paris.

Passelègue, F., A. Schubnel, S. Nielsen, H. S. Bhat, D. Deldicque, R. Madariaga, *et al.* (2016), Dynamic rupture processes inferred from laboratory microearthquakes, *Journal of Geophysical Research: Solid Earth,* doi:10.1002/2015JB012694.

Passelègue, F. X., A. Schubnel, S. Nielsen, H. S. Bhat, and R. Madariaga (2013), From sub-rayleigh to supershear ruptures during stick-slip experiments on crustal rocks, *Science*, *340*(6137), 1208–1211.

Rice, J. (1979), *The mechanics of earthquake rupture*, Division of Engineering, Brown University.

Ruina, A. (1983), Slip instability and state variable friction laws, *Journal of Geophysical Research: Solid Earth (1978–2012)*, *88*(B12), 10,359–10,370.

Ruiz, S., M. Metois, A. Fuenzalida, J. Ruiz, F. Leyton, R. Grandin, C. Vigny, R. Madariaga, and J. Campos (2014), Intense foreshocks and a slow slip event preceded the 2014 Iquique Mw 8.1 earthquake, *Science*, *345*(6201), 1165–1169.

Sammonds, P., P. Meredith, and I. Main (1992), Role of pore fluids in the generation of seismic precursors to shear fracture, *Nature*, *359*(6392), 228–230.

Schubnel, A., S. Nielsen, J. Taddeucci, S. Vinciguerra, and S. Rao (2011), Photo-acoustic study of subshear and supershear ruptures in the laboratory, *Earth and Planetary Science Letters*, *308*, 424 – 432, doi:10.1016/j.epsl.2011.06.013 .

Stirling, M. W., S. G. Wesnousky, and K. Shimazaki (1996), Fault trace complexity, cumulative slip, and the shape of the magnitude-frequency distribution for strike-slip faults: A global survey, *Geophysical Journal International*, *124*(3), 833–868.

Svetlizky, I., and J. Fineberg (2014), Classical shear cracks drive the onset of dry frictional motion, *Nature*, *509*, 205–208.

Thompson, B. D., R. P. Young, and D. A. Lockner (2009), Premonitory acoustic emissions and stick-slip in natural and smooth-faulted westerly granite, *J. Geophys. Res.*, *114*, B02205.

Uenishi, K., and J. R. Rice (2003), Universal nucleation length for slip-weakening rupture instability under nonuniform fault loading, *Journal of Geophysical Research: Solid Earth (1978–2012)*, *108*(B1).

Wong, T.-f. (1982), Shear fracture energy of Westerly granite from post-failure behavior, *Journal of Geophysical Research: Solid Earth (1978–2012)*, *87*(B2), 990–1000.

Wong, T.-F. (1986), On the normal stress dependence of the shear fracture energy, *Earthquake Source Mechanics*, pp. 1–11.

Zang, A., F. C. Wagner, S. Stanchits, G. Dresen, R. Andresen, and M. A. Haidekker (1998), Source analysis of acoustic emissions in aue granite cores under symmetric and asymmetric compressive loads, *Geophysical Journal International*, *135*(3), 1113–1130.